MASTER'S THESIS

Master of Science in Advanced Mathematics and Mathematical Engineering

Title: Numerical solution of phase-field models for two-phase flows

Author: Jordi Petchamé Guerrero

Advisors: Sonia Fernández-Méndez, Esther Sala Lardies

Department: Departament d'Enginyeria Civil i Ambiental

Academic year: 2021/2022

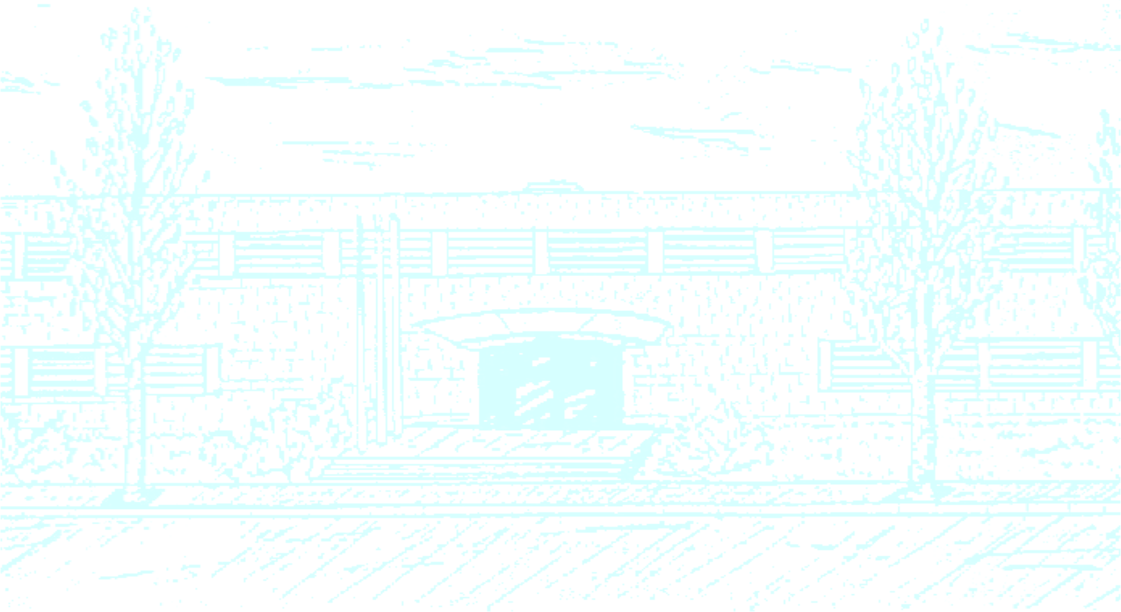

UNIVERSITAT POLITÈCNICA DE CATALUNYA
BARCELONATECH
Facultat de Matemàtiques i Estadística

Universitat Politècnica de Catalunya
Facultat de Matemàtiques i Estadística

Master in Advanced Mathematics and Mathematical Engineering
Master's thesis

Numerical solution of phase-field models for two-phase flows

Jordi Petchamé Guerrero

Supervised by Sonia Fernández-Méndez, Esther Sala Lardies

June, 2022

Thanks to my advisors Sonia Fernández-Méndez and Esther Sala Lardies for their guidance, knowledge and patience throughout the process.

Abstract

Phase-field models describe the motion of multiphase flows using smooth interfaces across which the composition changes continuously. The phase-field variable represents a measure of phase as it quantifies relative differences or fractions of the fluid's components. The Cahn-Hilliard equation was originally proposed to model spinodal decomposition and coarsening in binary alloys. To this day, it has become broad ranged in its applicability. This thesis focuses on solving the Cahn-Hilliard equation numerically. A review of the mathematical modelling is made in order to develop numerical methods. Different numerical simulations in two dimensions are implemented to study the numerical and physical properties. Two realistic physical examples are also numerically solved.

Keywords

Phase-field models, Cahn-Hilliard equation, two-phase flows, C^0-interior penalty method

Contents

1 Introduction **1**

2 Cahn-Hilliard equation **3**

3 Discretisation of the C^0-IPM weak form **6**

4 Numerical examples **8**

4.1 Synthetic example 8

4.2 Element size h in terms of γ 10

4.3 Influence of physical parameters 14

4.4 Phase separation 17

4.5 Potential flow 18

5 Conclusions **21**

1. Introduction

Multiphase flows are challenging to study due to the complexity of dealing with unknown moving interfaces, also known as free interfaces. One of the approaches to describe phase transition phenomena is known as *phase-field modelling*. Roughly speaking, the underlying idea is to replace sharp interfaces by thin transition regions of finite thickness with smooth distributions [9]. The interface-capturing approach is a way to implicitly capture the location of the interface by using a contour of a particular scalar function [11]. Phase-field models (also called diffuse-interface models [9, 17]) use this approach. They determine the evolution of material interfaces through the *phase-field variable* which characterises the phase distribution in space and time. In two-phase flows, it is related to the local concentrations of the two components involved. Usually it is measured as a rescaling of the difference between the two concentrations, but it can also be defined as the relative concentration of one of the components. Since it changes gradually through the thin layers that separate the different components, it enables the location of the interface.

The Cahn-Hilliard (CH) equation is a representative of this family of models. It describes the process of phase separation in multicomponent mixtures, and it captures implicitly the location of the interface in multiphase flow dynamics. It was originally proposed to model spinodal decomposition (i.e. the mechanism by which a single phase spontaneously separates into two distinct phases) in binary alloys [3, 4]. Its applications have been extended to a wide variety of phenomena, such as image inpainting [1, 2] or tumor growth simulation [16, 8], due to its capacity to describe qualitative features of many systems undergoing phase separation at different time stages [17]. In this thesis we mainly focus on the *advective* Cahn-Hilliard equation, in which the phase-field undergoes convection by a bulk velocity. As we will see in the next section, it is a fourth-order nonlinear partial differential equation for the phase-field, and it involves a chemical potential that models the immiscibility of the fluid's components.

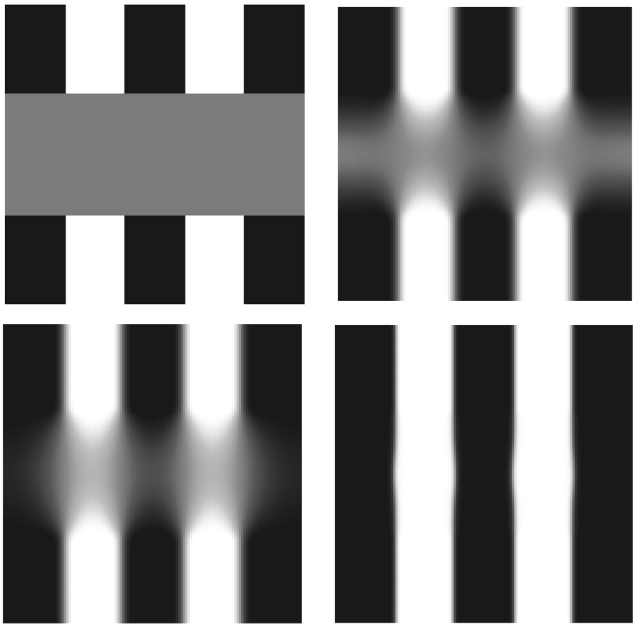

Figure 1: Image inpainting is the recovery of damaged images using information from surrounding areas. In this case, a modified CH equation is applied to recover the black and white stripes in the inpainting region in grey [12].

We can divide the objectives of this thesis in three steps. First, become familiar with the modelling of the advective CH equation, together with the associated boundary conditions and the meaning of the material parameters. Then, select and develop a numerical method, implement it and propose suitable candidates for the numerical parameters. Finally, illustrate realistic simulations of phase separation and bubble dynamics in a two-phase flow. For the sake of simplicity, our framework is the two-dimensional real space.

The structure of this thesis is organised as follows. The next section is an introduction to the mathematical modelling of the Cahn-Hilliard equation and its weak form with the C^0-interior penalty method [5, 6]. The discretisation in space and time is described in Section 3. Section 4 includes a series of numerical examples, divided into two synthetic examples and two realistic physical applications. The section begins with a spatial convergence test in a synthetic example of the steady CH equation in order to verify the accuracy and convergence of the C^0-IPM method. In the following two subsections, simulations of a rotating bubble in a two-phase flow are carried out. The first part focuses on proposing a candidate for the element size in our computational grids, in consideration of the interface thickness parameter. The second part studies the effect of the physical parameters in the evolution of the bubble. Regarding the physical applications, Subsection 4.4 describes and illustrates the phase separation process in a binary alloy that produces pattern formation. Finally, the last subsection portrays the motion of a bubble in a domain filled with obstacles, whereby the deformation of the interface is noteworthy.

This thesis has been implemented with MATLAB. To run simulations with large number of time steps, a cluster of the university has been used.

2. Cahn-Hilliard equation

Let $\Omega \in \mathbb{R}^2$ be a bounded domain. Let $u = u(\mathbf{x}, t)$ be the phase-field variable. The advective Cahn-Hilliard equation is given by

$$\frac{\partial u}{\partial t} + v \cdot \nabla u = \nabla \cdot \big(M(u) \nabla \mu(u)\big), \quad \mathbf{x} \in \Omega, t > 0, \tag{1}$$

with initial condition

$$u(\mathbf{x}, 0) = u_0(\mathbf{x}), \quad \mathbf{x} \in \Omega,$$

where u is the rescaled difference between the concentrations of the two components [11], the expression for μ is

$$\mu(u) = F'(u) - \gamma \Delta u, \tag{2}$$

and

$$F(u) = 0.25(u^2 - 1)^2. \tag{3}$$

In our setting, concentration is understood as a mass fraction. Mathematically speaking,

$$u = c_A - c_B, \quad c_A, c_B \in [0, 1], \quad c_A + c_B = 1.$$

We easily deduce from (3) that F is a double-well potential of a homogeneous system of composition u, as we can see in Figure 2. It has two minima at $u = \pm 1$, known as *binodal points* [9], which correspond to the fluid's two pure (or stable) phases. Moreover, v is the bulk velocity, $M(u)$ is the *degenerate mobility*[1] and $\sqrt{\gamma}$ controls the thickness of the transition interface. In this thesis we consider the simplified case where $M(u)$ is a positive constant D. As a result, (1) becomes a semilinear PDE.

The standard CH equation (i.e. without advection) arises from the Ginzburg-Landau free energy functional

$$\xi(u) = \int_\Omega \left(F(u) + \frac{\gamma}{2} |\nabla u|^2 \right) d\mathbf{x}. \tag{4}$$

The first contribution of (4) represents the interaction of different components in a homogeneous system, while the gradient contribution represents the spatial variation in composition of the mixture [17]. Following [14], the function μ represents the chemical potential that is derived from the variational derivative of the functional ξ with respect to the phase-field variable u. That is, for all $\nu \in H_0^1(\Omega)$,

$$\begin{aligned} \frac{d}{d\eta} \xi(u + \eta\nu) \bigg|_{\eta=0} &= \int_\Omega \big(\nu F'(u) + \gamma \nabla \nu \cdot \nabla u \big) \, d\mathbf{x} \\ &= \int_\Omega \big(F'(u) - \gamma \Delta u \big) \, \nu \, d\mathbf{x} + \int_{\partial\Omega} \gamma \frac{\partial u}{\partial \mathbf{n}} \nu \, ds \\ &= \int_\Omega \big(F'(u) - \gamma \Delta u \big) \, \nu \, d\mathbf{x}, \end{aligned}$$

where $\mathbf{n}$ is the outward pointing unit normal vector. The conserved dynamics of the CH equation is due to non-Fickian diffusion driven by gradients in the chemical potential [17]. Mass conservation implies

$$\frac{\partial u}{\partial t} + \nabla \cdot \mathcal{J} = 0$$

---

[1] Pure phases have no mobility.

where the flux is defined as $\mathcal{J} = -M(u)\nabla\mu$. This yields the explicit expression of the CH equation.

The model is based on the assumption of an isothermal and isotropic system. The thermodynamical foundations of the CH equation are beyond the scope of this thesis. For a thorough account of the physical and mathematical derivations of the CH equation, we refer the reader to [13, 17, 11].

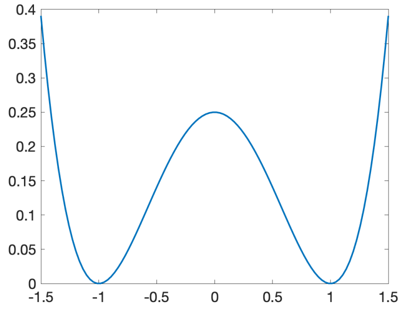

Figure 2: Double-well potential function $F(u)$.

The advective CH equation involves a fourth-order spatial partial differential operator. Thus, to derive the weak form we can multiply by a test function w and integrate by parts twice, obtaining

$$\begin{aligned}\int_\Omega w\frac{\partial u}{\partial t}d\mathbf{x} + \int_\Omega w(v\cdot\nabla u)d\mathbf{x} = &-D\int_\Omega \nabla w\cdot\nabla(u^3-u)d\mathbf{x} - D\gamma\int_\Omega \Delta w\Delta u\,d\mathbf{x}\\ &+D\int_{\partial\Omega} w\frac{\partial\mu}{\partial\mathbf{n}}ds + D\gamma\int_{\partial\Omega}\frac{\partial w}{\partial\mathbf{n}}\Delta u\,ds \qquad (5)\end{aligned}$$

for all $w \in H^2(\Omega)$, where

$$\frac{\partial\mu}{\partial\mathbf{n}} = \frac{\partial}{\partial\mathbf{n}}(u^3 - u - \gamma\Delta u).$$

The two boundary terms in (5) call for two boundary conditions that can be either Dirichlet or Neumann. They can be stated as

$$u = u_D \text{ on } \Gamma_D^1, \quad \frac{\partial\mu}{\partial\mathbf{n}} = t_N \text{ on } \Gamma_N^1, \quad \frac{\partial u}{\partial\mathbf{n}} = q \text{ on } \Gamma_D^2, \quad \Delta u = r_N \text{ on } \Gamma_N^2, \qquad (6)$$

with $\partial\Omega = \Gamma_D^1 \cup \Gamma_N^1 = \Gamma_D^2 \cup \Gamma_N^2$. The boundary condition on Γ_D^2 is counterintuitive from the standpoint of second-order PDEs since in this case it is a Dirichlet condition instead of Neumann.

In order to apply the finite element method (FEM) to the weak form (5) in $H^2(\Omega)$, the basis functions must be piecewise smooth and globally C^1-continuous. This becomes complicated when using unstructured grids. As a consequence, we use an alternative method called *C^0-interior penalty method* (C^0-IPM). This approach allows using standard C^0-continuous finite element basis functions by means of a variational formulation that assumes C^0-continuity and imposes both C^1-continuity and high-order interface conditions between elements.

Let us consider a partition of Ω in elements Ω_e, and let us denote the union of the interior sides of the mesh as

$$\Gamma = \left[\bigcup_e \partial\Omega_e\right] \setminus \partial\Omega$$

and the broken domain as

$$\hat{\Omega} = \bigcup_e \Omega_e.$$

According to [5, 6], the C^0-IPM bilinear form for the bilaplacian operator is

$$a(u, w) = D\gamma \int_{\hat{\Omega}} \Delta u \Delta w \, d\mathbf{x} + D \int_\Gamma \left[\left\llbracket \frac{\partial u}{\partial \mathbf{n}} \right\rrbracket \{\gamma \Delta w\} + \{\gamma \Delta u\} \left\llbracket \frac{\partial w}{\partial \mathbf{n}} \right\rrbracket \right] ds + D\beta \int_\Gamma \left\llbracket \frac{\partial u}{\partial \mathbf{n}} \right\rrbracket \left\llbracket \frac{\partial w}{\partial \mathbf{n}} \right\rrbracket \, ds, \quad (7)$$

where the jump and mean operators are respectively defined on interior sides as

$$\llbracket f \rrbracket = f^L \mathbf{n}^L + f^R \mathbf{n}^R, \quad \{f\} = \frac{1}{2}\left(f^L + f^R\right),$$

being f^L and f^R the values from the left and right elements sharing each side. The bilinear form (7) is symmetric and coercive provided the stabilisation parameter β is large enough. Moreover, the derivation of (7) assumes that u and w are in $H^2(\Omega_e) \cap H^1(\Omega)$ and that u satisfies interface conditions on the element sides.

The weak formulation for the advective Cahn-Hilliard equation (1) derived from the C^0-IPM bilinear form (7), assuming second Neumann conditions, is:

Find $u(\mathbf{x}, t)$ such that $u(\cdot, t) \in H^2(\Omega_e) \cap H^1(\Omega)\ \forall\, t > 0$, $u = u_D$ on Γ_D^1 and

$$\int_\Omega w \frac{\partial u}{\partial t} d\mathbf{x} + \int_\Omega w(v \cdot \nabla u) d\mathbf{x} = -D \int_\Omega \nabla w \cdot \nabla(u^3 - u) d\mathbf{x} - a(w, u) + \int_{\Gamma_N^1} w t_N \, ds + \int_{\Gamma_N^2} \frac{\partial w}{\partial \mathbf{n}} r_N \, ds \quad (8)$$

for all $w \in H^2(\Omega_e) \cap H^1(\Omega)$ such that $w = 0$ on Γ_D^1.

3. Discretisation of the C^0-IPM weak form

The finite element approximations considered are

$$u(\mathbf{x}) \simeq \mathbf{N}(\mathbf{x})\mathbf{u}, \quad u^3(\mathbf{x}) \simeq \mathbf{N}(\mathbf{x})\mathbf{u}^3, \quad w(\mathbf{x}) = \mathbf{N}(\mathbf{x}), \quad v(\mathbf{x}) \simeq \mathbf{N}(\mathbf{x}) \begin{bmatrix} \mathbf{v}^x \\ \mathbf{v}^y \end{bmatrix}, \tag{9}$$

with shape functions $\{N_i\}_{i=1}^m$, $\mathbf{N} = [N_1, \dots, N_m]$, where m is the number of nodes, and the vectors of nodal values $\mathbf{u} = [u_1, \dots, u_m]^T$, $\mathbf{u}^3 = [u_1^3, \dots, u_m^3]^T$. The gradient of u is therefore discretised as

$$\nabla u(\mathbf{x}) \simeq \nabla \mathbf{N}(\mathbf{x})\mathbf{u} = \begin{bmatrix} \frac{\partial \mathbf{N}}{\partial x}(\mathbf{x})\mathbf{u} & \frac{\partial \mathbf{N}}{\partial y}(\mathbf{x})\mathbf{u} \end{bmatrix}.$$

The discretisation of the weak form (8) leads to the following system of time-dependent ODEs:

$$\mathbf{M}\frac{\mathbf{du}}{\mathbf{dt}} = \mathbf{g}(\mathbf{u}) \tag{10}$$

with the mass matrix

$$\mathbf{M} = [m_{ij}], \quad m_{ij} = \int_\Omega N_i N_j \, d\mathbf{x},$$

and the nonlinear function

$$\mathbf{g}(\mathbf{u}) = -\mathbf{K}(\mathbf{u}^3 - \mathbf{u}) - \mathbf{D}\mathbf{u} - \mathbf{C}\mathbf{u} - \mathbf{f}, \tag{11}$$

where:

- $\mathbf{K} = [k_{ij}]$ is the stiffness matrix
$$k_{ij} = D \int_\Omega \nabla N_i \nabla N_j \, d\mathbf{x},$$
- $\mathbf{D} = [d_{ij}]$ is the matrix discretising the bilinear form (7)
$$d_{ij} = D\gamma \int_{\hat{\Omega}} \Delta N_i \Delta N_j \, d\mathbf{x} + D \int_\Gamma \left[\left[\!\left[\frac{\partial N_i}{\partial \mathbf{n}} \right]\!\right] \{\gamma \Delta N_j\} + \{\gamma \Delta N_i\} \left[\!\left[\frac{\partial N_j}{\partial \mathbf{n}} \right]\!\right] \right] ds + D\beta \int_\Gamma \left[\!\left[\frac{\partial N_i}{\partial \mathbf{n}} \right]\!\right] \left[\!\left[\frac{\partial N_j}{\partial \mathbf{n}} \right]\!\right] ds,$$
- $\mathbf{C} = [c_{ij}]$ is the advection matrix
$$c_{ij} = \int_\Omega N_i (v \cdot \nabla N_j) d\mathbf{x},$$
- $\mathbf{f}$ is the vector with the Neumann terms
$$f_i = D \int_{\Gamma_N^1} N_i t_N \, ds + D \int_{\Gamma_N^2} \frac{\partial N_i}{\partial \mathbf{n}} r_N \, ds. \tag{12}$$

All these matrices can be precomputed thanks to the second approximation in (9) which keeps the approximation error of the standard FEM [5].

To solve (10), we can use integration methods such as the *mid-point rule* which leads to a nonlinear system of equations

$$\mathbf{M}\frac{\mathbf{u}^{n+1} - \mathbf{u}^n}{\Delta t} = \mathbf{g}\left(\frac{\mathbf{u}^{n+1} + \mathbf{u}^n}{2}\right), \quad n = 0, 1, 2, \dots$$

to be solved in each time step $t^n = n\Delta t$, to compute $\mathbf{u}^{n+1} \simeq \mathbf{u}(t^{n+1})$ from $\mathbf{u}^n \simeq \mathbf{u}(t^n)$ for all n. The system can be written as $\mathbf{r}(\mathbf{u}^{n+1}) = 0$ with the residual

$$\mathbf{r}(\mathbf{u}) = \mathbf{M}(\mathbf{u} - \mathbf{u}^n) - \Delta t \ \mathbf{g}\left(\frac{\mathbf{u} + \mathbf{u}^n}{2}\right).$$

Since the problem is reduced to finding the solution of $\mathbf{r}(\mathbf{u}^{n+1}) = 0$, we apply Newton's method with the jacobian matrix

$$\mathbf{J}(\mathbf{u}) = \frac{\mathbf{dr}}{\mathbf{du}} = \mathbf{M} + \frac{\Delta t}{2}\left(\mathbf{K}\boldsymbol{\Lambda}\left(\frac{\mathbf{u} + \mathbf{u}^n}{2}\right) + \mathbf{D} + \mathbf{C}\right),$$

where $\boldsymbol{\Lambda}(\mathbf{u})$ is a diagonal matrix with coefficients $\lambda_{ii} = 3u_i^2 + 1$. Another possible method is the *second-order trapezoidal rule*, given by

$$\mathbf{M}\frac{\mathbf{u}^{n+1} - \mathbf{u}^n}{\Delta t} = \frac{1}{2}\left(\mathbf{g}(\mathbf{u}^{n+1}) + \mathbf{g}(\mathbf{u}^n)\right), \quad n = 0, 1, 2, \ldots.$$

This method is more computationally costly, since we are computing (11) twice at each time iteration. For this reason, we choose the mid-point rule in our implementation.

4. Numerical examples

The mathematical and numerical frameworks described in the previous sections lead us to run numerical simulations of physical phenomena in different settings. The first step is to verify the efficacy of the C^0-interior penalty method. This step is fundamental in order to obtain reliable results. The next step is to identify suitable numerical parameters that will be used in applications. The key aspect is to understand the degree of dependence on the physical parameters. Once these two requirements are met, we apply our methods to reproduce realistic physical scenarios.

In all numerical tests, the computational meshes are composed of triangular elements.

4.1 Synthetic example

We consider a synthetic example of the steady Cahn-Hilliard equation to test convergence in space. We are only interested in checking that the orders of convergence are in agreement with the theoretical predictions. Hence, the physical parameters are set to 1 and no physical interpretations are made.

Let $u = u(x, y)$ and $\Omega = (0, 1) \times (0, 1)$. Since $D = \gamma = 1$, then from (2) and (3) we have

$$\mu(u) = u^3 - u - \Delta u.$$

The boundary-value problem is

$$\begin{cases} \Delta\mu = f_{an}, & \text{in } \Omega, \\ u = u_{an}, & \text{on } \partial\Omega, \\ \Delta u = \Delta u_{an}, & \text{on } \partial\Omega, \end{cases} \tag{13}$$

where

$$u_{an} = \sin(2\pi(x + y)) \tag{14}$$

is the analytical solution (see Figure 3) and

$$f_{an} = -8\pi^2 \left(8\pi^2 - 9\cos\left(2\pi(x + y)\right)^2 + 2\right) \sin\left(2\pi(x + y)\right)$$

is the analytical source term. It is easy to deduce from (14) that

$$\Delta u_{an} = -8\pi^2 \sin\left(2\pi(x + y)\right).$$

The first boundary condition in (13) is Dirichlet, whereas the second one is Neumann. The system to solve is

$$\tilde{\mathbf{g}}(\mathbf{u}) = 0$$

with

$$\tilde{\mathbf{g}}(\mathbf{u}) = -\mathbf{K}(\mathbf{u}^3 - \mathbf{u}) - \mathbf{D}\mathbf{u} - \mathbf{f} + \mathbf{M}\mathbf{f}_{an}.$$

The vector $\mathbf{f}_{an}$ contains the nodal values of f_{an}. Moreover, the Neumann terms (12) are

$$f_i = \int_{\partial\Omega} \frac{\partial N_i}{\partial \mathbf{n}} \Delta \mathbf{u}_{an}\, ds.$$

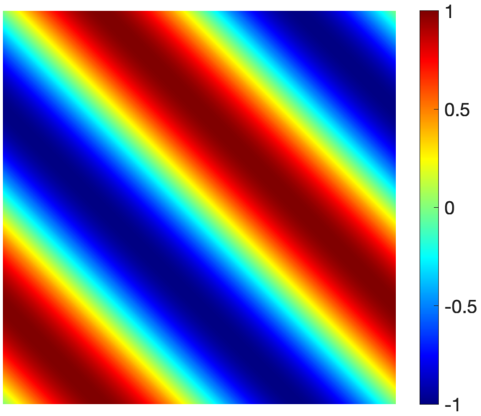

Figure 3: Analytical solution u_{an}.

Since we have used finite elements to discretise in space, we expect that the L^2-error converges with order $O\left(h^{p+1}\right)$, p being the degree of approximation [15, Section 4.5]. Figure 4 shows convergence in space for

$$h = \frac{1}{2^i}, \quad i = 1, 2, 3, 4, 5.$$

Following the recommendations in [6], we use $\beta = 100/h$ to achieve optimal convergence for $p \geq 3$. In agreement also with [6], approximations of degree 4 are less sensitive to parameters. Consequently, we choose elements of degree 4 in all the remaining numerical examples.

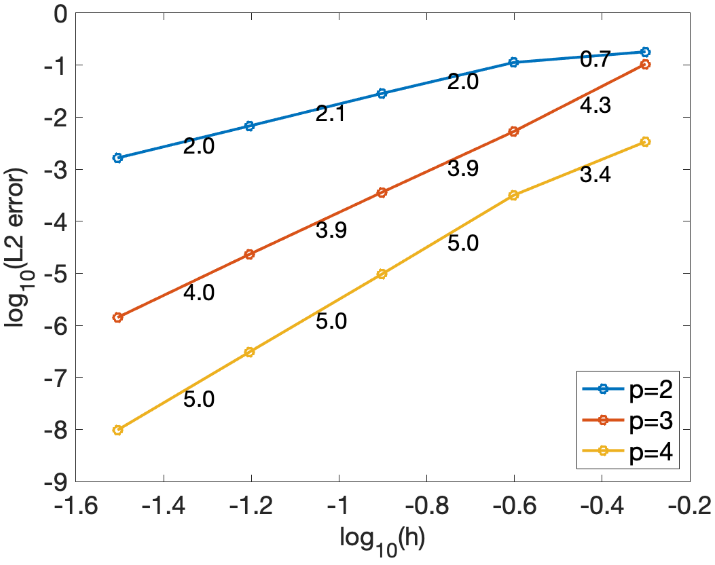

Figure 4: Convergence plots for different degrees p. The numbers represent the slopes of the segments.

4.2 Element size h in terms of γ

Once the accuracy and convergence of our spatial discretisation method has been verified, we turn our attention to finding suitable numerical parameters for our physical examples. The previous subsection justifies the choice of an approximation with degree 4. Regarding the mesh, it must be fine enough to capture the smooth variation in the interface, but as coarse as possible to reduce computational cost. Thus, the level of domain resolution that is required is clearly dependent on the thickness of the interface, controlled by the parameter γ. In [7], the following criterion is considered for a linear approximation:

$$1 \leq \frac{h}{\sqrt{\gamma}} \leq 2.$$

The authors choose $h = \sqrt{\gamma}$ corresponding to the smallest element size. Thus, for degree $p = 4$, the candidate for the element size is $h^* = 4\sqrt{\gamma}$. In order to adjust this value to the mesh, we compute the number of elements in one dimension, $N = \lceil 1/h^* \rceil$, and then we obtain the new value of the mesh size $h = 1/N$.

The following two subsections present numerical results of a rotating bubble governed by the advective Cahn-Hilliard equation. The domain is the unit square $\Omega = (0,1) \times (0,1)$ and we impose first Dirichlet and second Neumann boundary conditions:

$$u_D = -1, \quad \Delta u = 0 \quad \text{on } \partial\Omega.$$

The initial condition is a smooth square bubble defined by

$$u_0(x,y) = 2 f_{IC}(x - 0.25) f_{IC}(y - 0.5) - 1$$

with $f_{IC}(z) = e^{-1000z^4}$.[2] In Figure 5 we see clearly the thin layers in the interface with intermediate values between the two pure phases ±1. The choice of this initial condition lies in our interest in observing the smoothening role of diffusion in the advective CH equation. Moreover, the rotating velocity field is

$$v = V\left(-(y - 0.5), x - 0.5\right), \quad V > 0.$$

Henceforth, we assume $V = 10$.

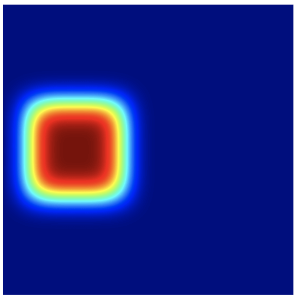

Figure 5: Initial condition u_0.

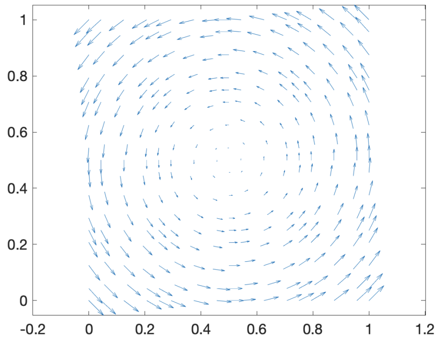

Figure 6: Directions of the velocity field v.

---

[2] Notice that this function is similar to the standard Dirac delta function.

Figures 7-9 show the position of the bubble at $t = 0.25$ for $D = 0.01$ and[3]

$$\gamma = 10^{-4}, 4 \cdot 10^{-3}, 10^{-3}.$$

There is a significant increase in accuracy when we refine the mesh from $2h^*$ to h^*. For this reason we discard the former mesh size. On the other hand, the results are nearly identical for h^* and $h^*/2$. We can safely conclude that h^* provides a reasonably accurate approximation of the solutions in this example, at least with respect to $h^*/2$.

In contrast, we cannot give a general recommendation in terms of the optimal time step. Besides the mesh size and parameters, it also depends on the example in hand. The value $\Delta t = 10^{-3}$ has been found to be small enough so that the results are not significantly altered. Unless otherwise stated, this time step is used in every simulation henceforth.

As a remark, due to computational limitations, values of γ smaller than 10^{-4} have not been considered in this thesis.

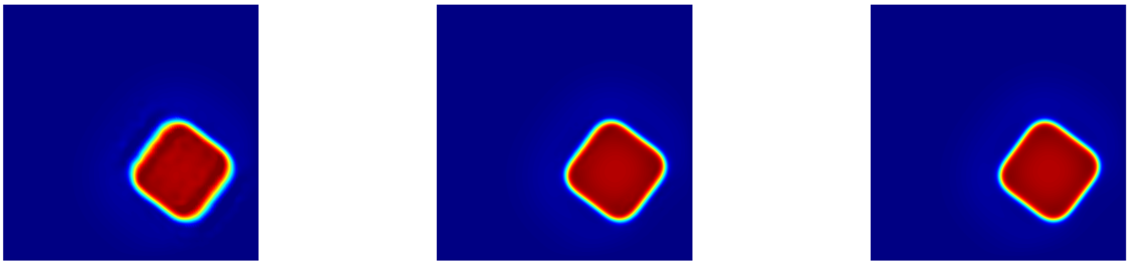

(a) $h = 1/13 \simeq 0.076923$.

(b) $h = 0.04$.

(c) $h = 0.02$.

Figure 7: Plots for $2h^*$, h^* and $h^*/2$ with $\gamma = 10^{-4}$, $h^* = 0.04$.

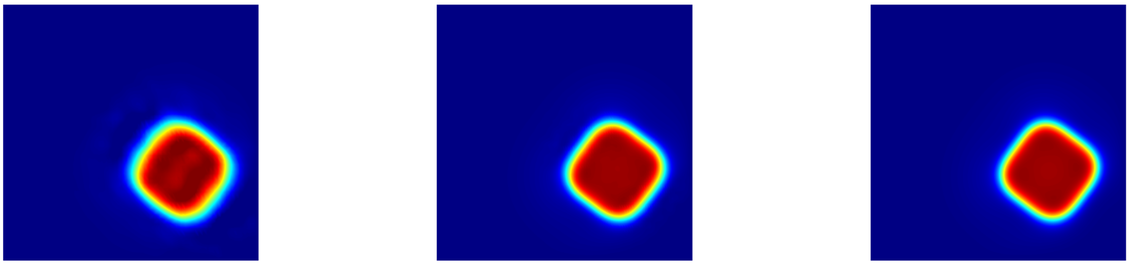

(a) $h = 1/7 \simeq 0.142857$.

(b) $h = 1/13 \simeq 0.076923$.

(c) $h = 0.04$.

Figure 8: Plots for $2h^*$, h^* and $h^*/2$ with $\gamma = 4 \cdot 10^{-4}$, $h^* = 0.08$.

---

[3] All the parameter values are chosen *ad hoc* for the sake of numerical interpretations.

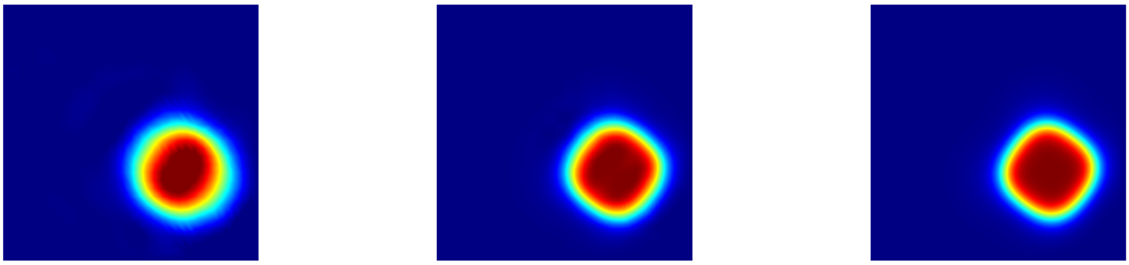

(a) $h = 0.25$.

(b) $h = 0.125$.

(c) $h = 0.0625$.

Figure 9: Plots for $2h^*$, h^* and $h^*/2$ with $\gamma = 10^{-3}$, $h^* \simeq 0.126491$.

The same analysis is shown now for the increasing values of γ considered before, but now with diffusion depending on the interface thickness. More precisely, $D = \sqrt{\gamma}$, inspired by the necessary condition for diffusion to dominate over convective distortion

$$D = O\left(\gamma^{\delta/2}\right), \quad 1 \leq \delta < 2, \tag{15}$$

claimed in [10]. The same conclusions as before can be drawn from Figures 10-12.

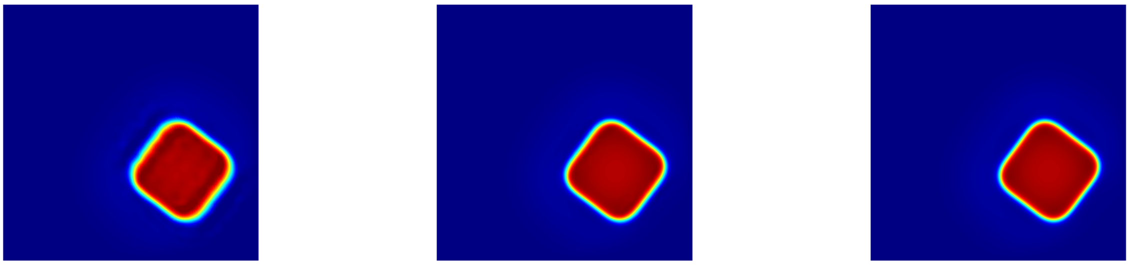

(a) $h = 1/13 \simeq 0.076923$.

(b) $h = 0.04$.

(c) $h = 0.02$.

Figure 10: Plots for $2h^*$, h^* and $h^*/2$ with $\gamma = 10^{-4}$, $h^* = 0.04$.

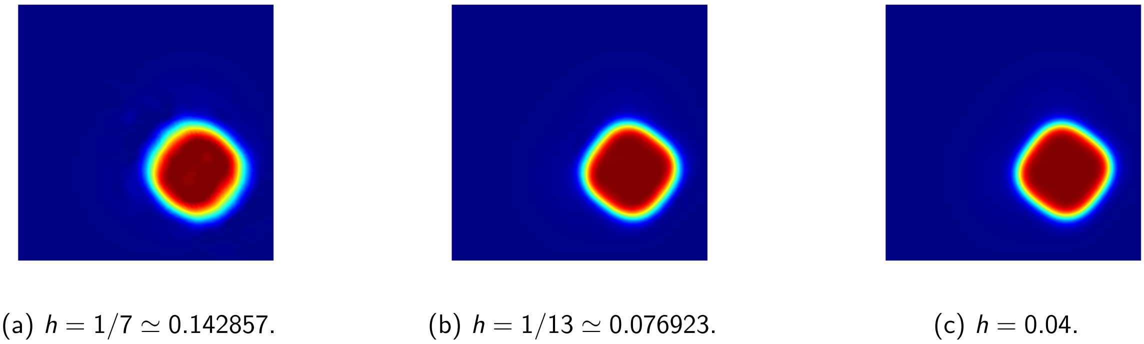

(a) $h = 1/7 \simeq 0.142857$.

(b) $h = 1/13 \simeq 0.076923$.

(c) $h = 0.04$.

Figure 11: Plots for $2h^*$, h^* and $h^*/2$ with $\gamma = 4 \cdot 10^{-4}$, $h^* = 0.08$.

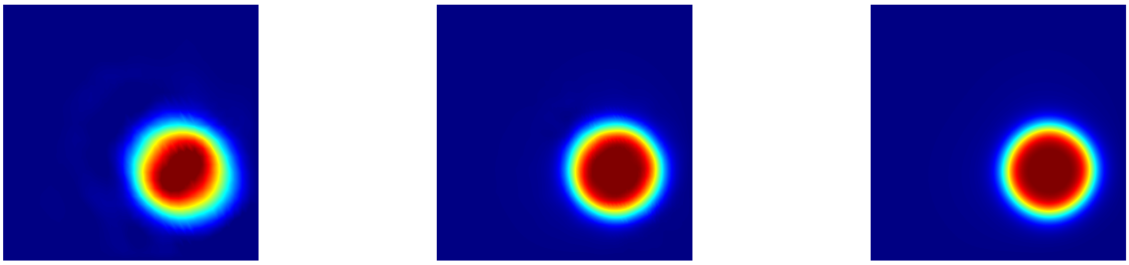

(a) $h = 0.25$.

(b) $h = 0.125$.

(c) $h = 0.0625$.

Figure 12: Plots for $2h^*$, h^* and $h^*/2$ with $\gamma = 10^{-3}$, $h^* \simeq 0.126491$.

4.3 Influence of physical parameters

Let us shift focus towards the physics of the problem. Within the numerical framework established in the previous subsection, that is, taking $h^* = 4\sqrt{\gamma}$ and $\Delta t = 10^{-3}$, we study the effects of increasing the diffusion coefficient D for a given value of γ. This parameter must be chosen so as to have a suitable time scale of diffusion. The diffusion coefficient must be large enough to resist straining flows that can thin or thicken the interface, but not too big that it overly damps the flow [7]. In a sense, it measures how fast the interface changes.

We want to see for which value of γ diffusion starts to change the shape of the moving bubble with respect to the initial condition. We fix the same values of γ as in Subsection 4.2 and we run our code for increasing values of D. To see a nearly full rotation of the bubble around the centre of the domain, we stop the process at $t = 0.5$.

Figures 13-15 show that an increase in γ requires less diffusion to gradually transform the shape of the bubble into a circle. Moreover, in Figures 16-18 we observe that an increase in diffusion results in a faster smoothening of the initial shape. Furthermore, as the interface becomes thicker, the surface of the positive pure phase slowly diminishes over time.

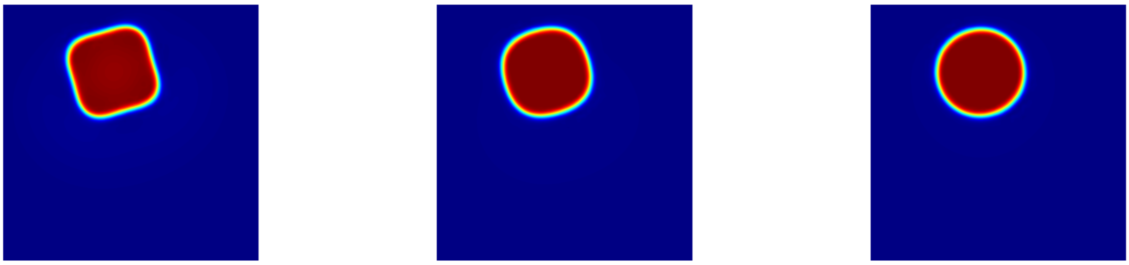

(a) $D = 10^{-2}$. (b) $D = 4 \cdot 10^{-2}$. (c) $D = 10^{-1}$.

Figure 13: Plots for different values of D with $\gamma = 10^{-4}$, $h = 0.04$.

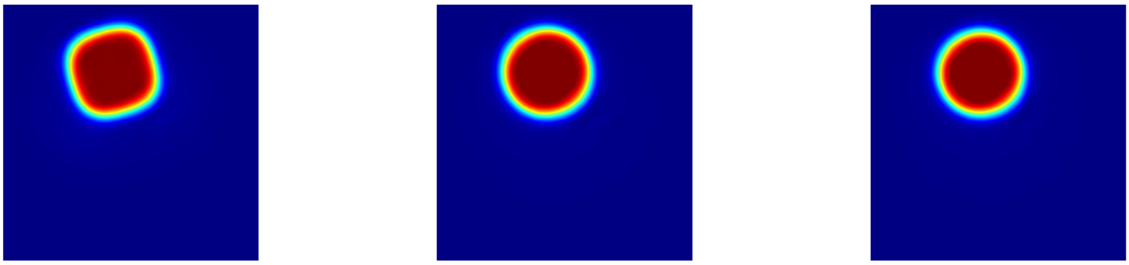

(a) $D = 10^{-2}$. (b) $D = 4 \cdot 10^{-2}$. (c) $D = 10^{-1}$.

Figure 14: Plots for different values of D with $\gamma = 4 \cdot 10^{-4}$, $h \simeq 0.076923$.

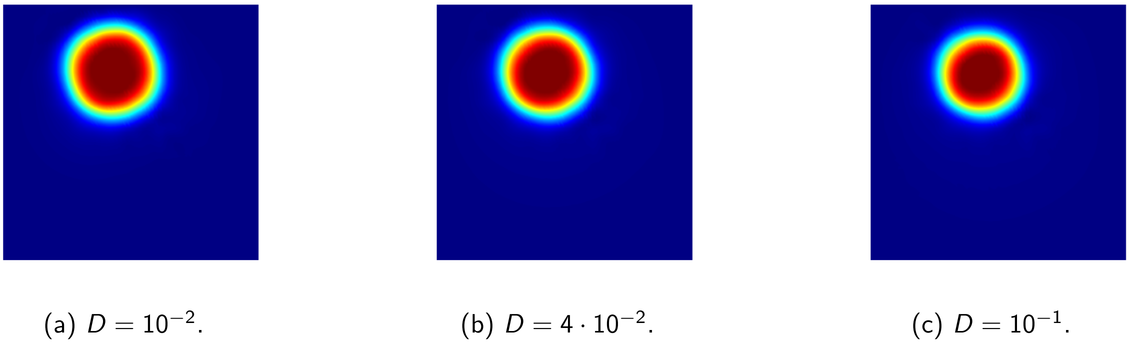

(a) $D = 10^{-2}$.

(b) $D = 4 \cdot 10^{-2}$.

(c) $D = 10^{-1}$.

Figure 15: Plots for different values of D with $\gamma = 10^{-3}$, $h = 0.125$.

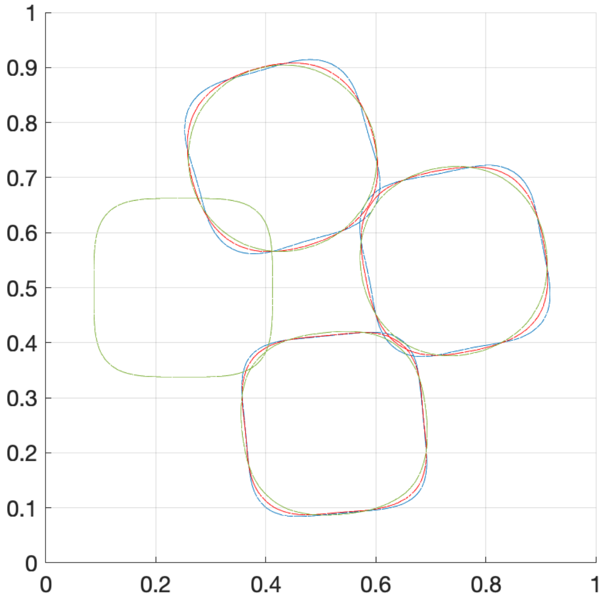

Figure 16: Contour plots of Figure 13. The blue shapes correspond to $D = 10^{-2}$, the red shapes to $D = 4 \cdot 10^{-2}$ and the green shapes to $D = 10^{-1}$. The time instants are $t = 0, 0.167, 0.334, 0.5$.

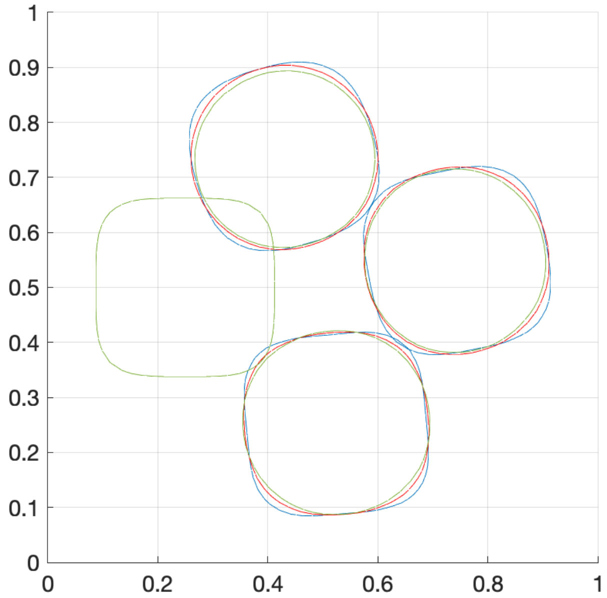

Figure 17: Contour plots of Figure 14.

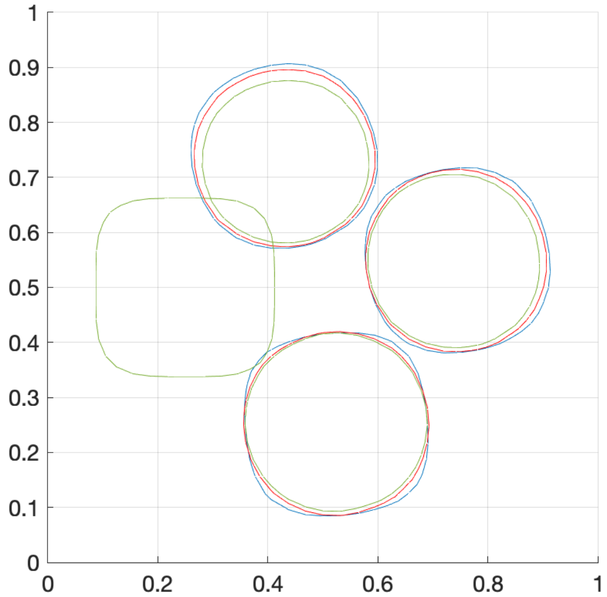

Figure 18: Contour plots of Figure 15.

4.4 Phase separation

The standard Cahn-Hilliard equation is solved with the same domain and boundary conditions as in Subsection 4.2. The interest of this subsection lies in reproducing spinodal decomposition in a binary alloy as a realistic example of phase separation. In this setting, a random initial distribution with values between the two pure phases ± 1 is considered. The aim is to visualise the process whereby the two components spontaneously separate into different regions where the phase-field variable reaches the pure phases, and then, these intertwined domains undergo coarsening. The separation process is due to the minimisation of the potential $F(u)$, which drives the concentrations to the binodal points. On the other hand, the minimisation of the gradient energy in (4)

$$\int_{\Omega} \frac{\gamma}{2} |\nabla u|^2 \, d\mathbf{x}$$

causes the coarsening process, with a larger time scale than the previous process [9]. This is illustrated in Figure 19.

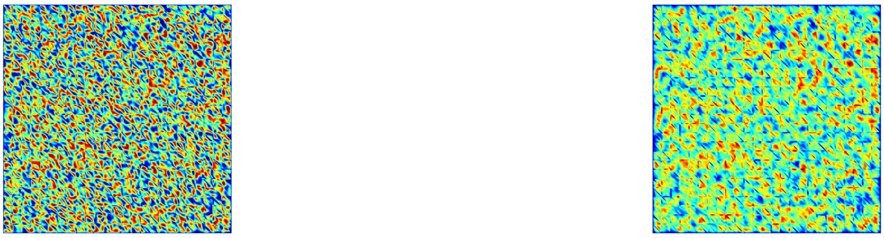

(a) Initial condition.

(b) $t = 0.0005$.

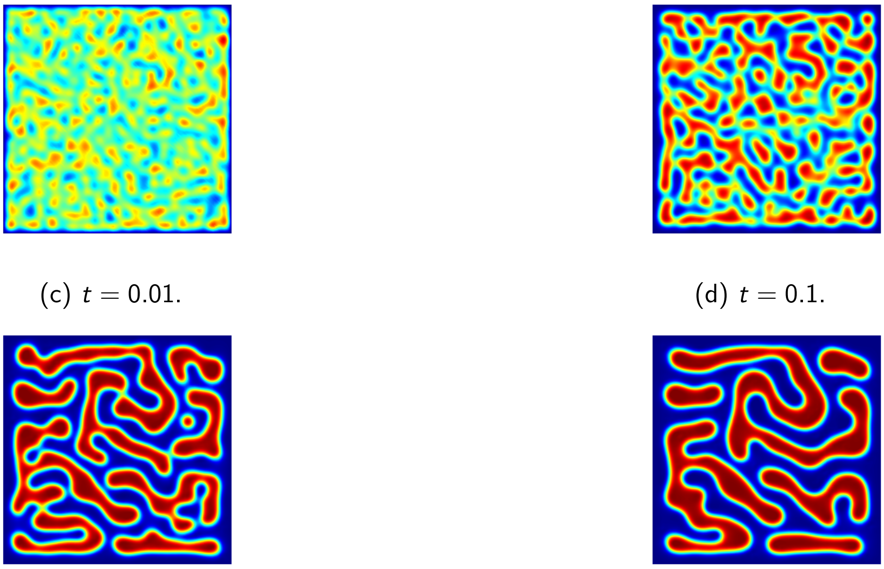

(c) $t = 0.01$.

(d) $t = 0.1$.

(e) $t = 0.5$.

(f) $t = 1$.

Figure 19: Evolution of a binary alloy from a random initial condition. The parameters are $\gamma = 10^{-4}$, $D = 0.01$, $h = 0.04$, $\Delta t = 10^{-4}$.

4.5 Potential flow

The last part of this project is a study of the behaviour of a two-phase potential flow under the action of the advective Cahn-Hilliard equation in a domain with obstacles. More precisely, we include various circles within a rectangle, and we simulate the motion of a smooth bubble in our phase-field model. The idea is to compute the velocity of the potential flow and apply it in (1).

Let us recall the basics of potential flow theory. A flow is incompressible if its velocity field has zero divergence. The vorticity field of a flow is defined as the curl of the velocity field. An irrotational flow is defined as having zero vorticity. This leads to the definition of a potential flow: an inviscid, irrotational flow. Moreover, there exists a scalar function ϕ known as *velocity potential* such that the velocity field can be expressed as

$$v = \nabla\phi.$$

It follows that the velocity potential satisfies the Laplace equation

$$\Delta\phi = 0.$$

We fix the rectangle $(0, 10) \times (0, 3)$ as our initial domain, and we insert three circles of different radii to obtain the new domain with obstacles, Ω_{ob}. Moreover, we set the Dirichlet conditions

$$\begin{cases} \phi = 0 & \text{for } x = 0, \\ \phi = 10 & \text{for } x = 10, \end{cases}$$

and impermeable conditions elsewhere. Let us denote the Dirichlet boundary by

$$\Gamma_D = \overline{\Omega_{ob}} \cap \big(\{x = 0\} \cup \{x = 10\}\big)$$

and the Neumann boundary by $\Gamma_N = \overline{\Omega_{ob}} \setminus \Gamma_D$. The problem can be written as

$$\begin{cases} \Delta\phi = 0 & \text{in } \Omega_{ob}, \\ \phi = x & \text{on } \Gamma_D, \\ \nabla\phi \cdot \mathbf{n} = 0 & \text{on } \Gamma_N. \end{cases} \tag{16}$$

Once we have obtained the velocity potential ϕ, we can compute the velocity field $v = \nabla\phi$ and use it in (1). To see the trajectories, we can compute the stream function φ given by

$$\begin{cases} \Delta\varphi = 0 & \text{in } \Omega_{ob}, \\ \frac{\partial\varphi}{\partial\mathbf{n}} = \mathbf{n} \cdot (v_y, -v_x) & \text{on } \partial\Omega_{ob}. \end{cases}$$

Since $\nabla\varphi \cdot v = 0$, the trajectories (or *streamlines*) are the level curves of φ. Figure 20 illustrates a collection of them.

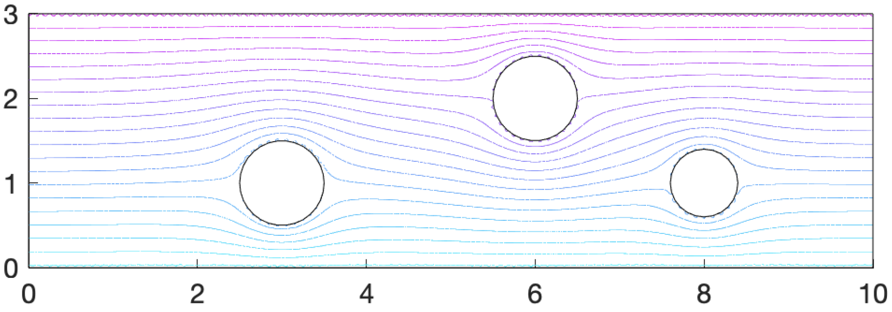

Figure 20: Streamlines of the flow.

We consider an unstructured grid adapted to the domain Ω_{ob}, as Figure 21 shows. Problem (16) can be solved numerically with the standard FEM since it is a second-order elliptic PDE (see [15, Chapter 4] for a rigorous description). The velocity field can be computed by means of the gradient smoothing method. In order to have a smooth initial condition, we set $\gamma = 6 \cdot 10^{-4}$ based on the range of values we have dealt with in the previous subsections. Since the candidate for the element size is $h^* = 4\sqrt{\gamma} \simeq 0.098$, we fix $h = 0.1$. Moreover, we take $D = \sqrt{\gamma} \simeq 0.0245$ following the relation in (15).

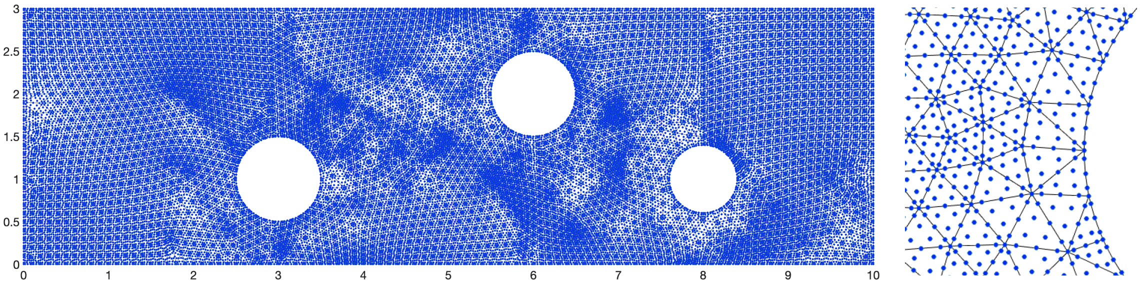

Figure 21: Domain Ω_{ob}.

To run a simulation of this process, we consider a bubble with phase 1, immersed in a fluid with phase -1. As in the previous section, the interface is smooth and comprised of thin layers valued between the pure phases. The expression for the initial condition is

$$u_0(x, y) = 2f_{IC}\left((x-1)^2 + (y-2)^2\right) - 1.$$

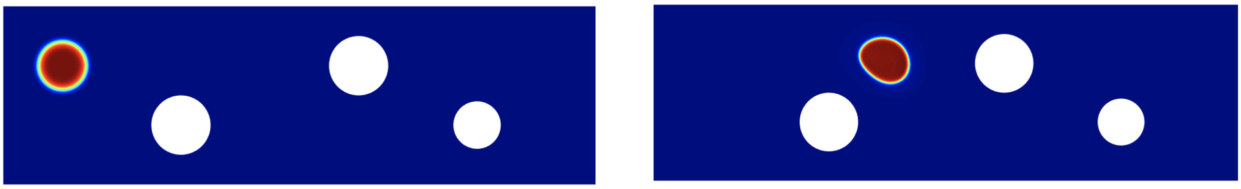

(a) Initial condition.

(b) $t = 0.3$.

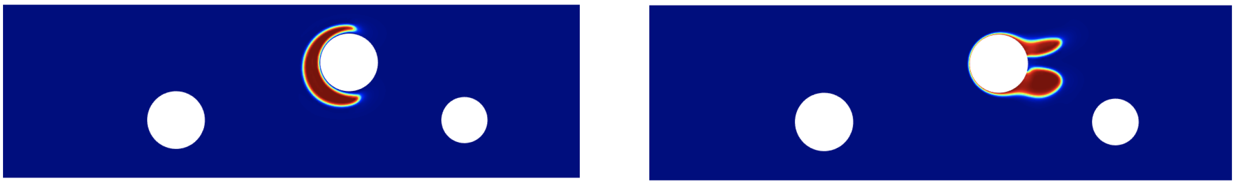

(c) $t = 0.5$.

(d) $t = 0.6$.

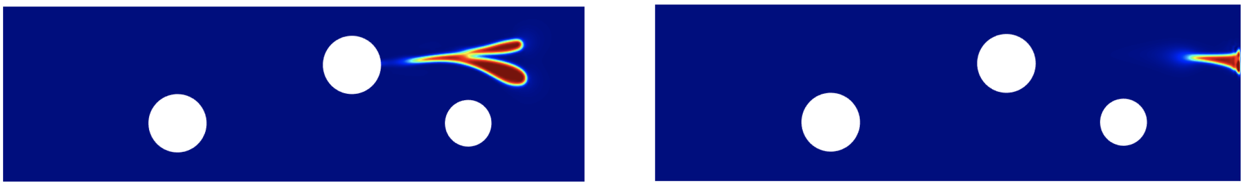

(e) $t = 0.8$.

(f) $t = 1$.

Figure 22: Evolution of a bubble in a two-phase potential flow passing through an obstacle.

We observe in Figure 22 that the bubble follows the streamlines, surrounds the obstacle and then splits in two parts before reaching the boundary. The bubble is deformed as a result of the velocity field. Notice also that the layers within the interface change in shape but not in phase. In other words, the smoothness of the interface remains intact.

5. Conclusions

This thesis serves as an introduction to phase-field models through the Cahn-Hilliard equation. The conclusions can be divided in the same way as the objectives.

The modelling of the advective CH equation with boundary conditions and the subsequent weak formulation has been elaborated in Section 2, including a brief physical derivation and a physical interpretation of the parameters.

To obtain numerical solutions of the CH equation, a modification of the standard finite element method, suitable for fourth-order PDEs, has been introduced. In addition, two similar time integration methods have been compared to select the most convenient one. The candidate for the mesh size has been claimed and justified, as well as an efficient and robust degree of approximation.

For the sake of having a better understanding of this model, numerical examples of the standard and advective CH equations have been included. In a simple model of a two-phase flow in a two-dimensional unit square, convergence of the C^0-IPM method has been proved to be in agreement with the theory by means of a synthetic example of the steady CH equation. Simulations of bubble dynamics have enabled us to analyse the influence of the physical parameters on the results. On this matter, the counterbalance between diffusion and interface thickness has been graphically shown. Finally, to broaden the scope of this thesis, one application of the standard CH equation and one application of the advective CH equation have been illustrated. First, the process of phase segregation from a random initial condition. Second, the motion of a bubble following the streamlines of a potential flow passing through an obstacle.

In all these simulations, the usefulness of the different forms of the CH equation has been illustrated. Moreover, the results have been consistent with the prior expectations, both from the numerical and physical standpoints.

As a future work, it would be interesting to consider non-constant mobility in the CH equation. Examples would be $M(u) = Du(1-u)$, where D represents diffusivity [9], or $M(u) = 1 - u^2$ [17]. It could also be interesting to impose different boundary conditions at the obstacles in the domain considered in Subsection 4.5.

Another future direction might be to use adaptive mesh refinement. Regions with pure phases can be discretised with coarse meshes without losing accuracy. Therefore, a grid refined only at the interface would be more computationally efficient.

References

[1] Andrea Bertozzi, Selim Esedoglu, and Alan Gillette. Analysis of a Two-Scale Cahn-Hilliard Model for Binary Image Inpainting. *Multiscale Modeling & Simulation*, 6(3), 2007.

[2] Antun Lovro Brkić, Darko Mitrović, and Andrej Novak. On the image inpainting problem from the viewpoint of a nonlocal Cahn-Hilliard type equation. *Journal of Advanced Research*, 25, 2020.

[3] John W. Cahn. On spinodal decomposition. *Acta Metallurgica*, 9(9), 1961.

[4] John W. Cahn and John E. Hilliard. Free energy of a nonuniform system. I. Interfacial free energy. *The Journal of Chemical Physics*, 28(2), 1958.

[5] Sonia Fernández-Méndez. C0 interior penalty FE solution of the Cahn-Hilliard equation. 2022.

[6] Dani Fojo, David Codony, and Sonia Fernández-Méndez. A C^0 Interior Penalty Method for 4^{th} order PDEs. *Reports@SCM*, 2020.

[7] Harish Ganapathy, Ebrahim Al-Hajri, and Michael M. Ohadi. Phase Field Method for Simulation of Multiphase Flow. In *Proceedings Of The ASME 2011 International Mechanical Engineering Congress & Exposition*, November 2011.

[8] Harald Garcke, Kei Fong Lam, Robert Nürnberg, and Emanuel Sitka. A multiphase Cahn-Hilliard-Darcy model for tumour growth with necrosis. *Mathematical Models and Methods in Applied Sciences*, 28(3), 2018.

[9] Héctor Gómez, Victor M. Calo, Yuri Bazilevs, and Thomas J.R. Hughes. Isogeometric analysis of the Cahn-Hilliard phase-field model. *Computer Methods in Applied Mechanics and Engineering*, 197(49), 2008.

[10] David Jacqmin. Calculation of Two-Phase Navier-Stokes Flows Using Phase-Field Modeling. *Journal of Computational Physics*, 155(1), 1999.

[11] Junseok Kim. Phase-Field Models for Multi-Component Fluid Flows. *Communications in Computational Physics*, 12(3), 2012.

[12] Junseok Kim, Seunggyu Lee, Yongho Choi, Seok-Min Lee, and Darae Jeong. Basic Principles and Practical Applications of the Cahn-Hilliard Equation. *Mathematical Problems in Engineering*, 2016.

[13] Dongsun Lee, Joo-Youl Huh, Darae Jeong, Jaemin Shin, Ana Yun, and Junseok Kim. Physical, mathematical and numerical derivations of the Cahn-Hilliard equation. *Computational Materials Science*, 81, 2014.

[14] Yibao Li, Darae Jeong, Jaemin Shin, and Junseok Kim. A conservative numerical method for the Cahn-Hilliard equation with Dirichlet boundary conditions in complex domains. *Computers & Mathematics with Applications*, 65, 2013.

[15] Alfio Quarteroni. *Numerical Models for Differential Problems*, volume 8. Springer, second edition, 2014.

[16] S.M. Wise, J.S. Lowengrub, H.B. Frieboes, and V. Cristini. Three-dimensional multispecies nonlinear tumor growth-I: Model and numerical method. *Journal of Theoretical Biology*, 253(3), 2008.

[17] Hao Wu. A Review on the Cahn-Hilliard Equation: Classical Results and Recent Advances in Dynamic Boundary Conditions, 2021.